Large-scale optimal transport map estimation using projection pursuit

Cheng Meng[1] **Yuan Ke**[1] **Jingyi Zhang**[1] **Mengrui Zhang**[1] **Wenxuan Zhong**[1] **Ping Ma**[1]

[1]Department of Statistics, University of Georgia
{cheng.meng25, yuan.ke, jingyi.zhang25, mengrui.zhang, wenxuan, pingma }@uga.edu

Abstract

This paper studies the estimation of large-scale optimal transport maps (OTM), which is a well known challenging problem owing to the curse of dimensionality. Existing literature approximates the large-scale OTM by a series of one-dimensional OTM problems through iterative random projection. Such methods, however, suffer from slow or none convergence in practice due to the nature of randomly selected projection directions. Instead, we propose an estimation method of large-scale OTM by combining the idea of projection pursuit regression and sufficient dimension reduction. The proposed method, named projection pursuit Monge map (PPMM), adaptively selects the most "informative" projection direction in each iteration. We theoretically show the proposed dimension reduction method can consistently estimate the most "informative" projection direction in each iteration. Furthermore, the PPMM algorithm weakly convergences to the target large-scale OTM in a reasonable number of steps. Empirically, PPMM is computationally easy and converges fast. We assess its finite sample performance through the applications of Wasserstein distance estimation and generative models.

1 Introduction

Recently, optimal transport map (OTM) draws great attention in machine learning, statistics, and computer science due to its close relationship to generative models, including generative adversarial nets [19], the "decoder" network in variational autoencoders [27], among others. In a generative model, the goal is usually to generate a "fake" sample, which is indistinguishable from the genuine one. This is equivalent to find a transport map ϕ from random noises with distribution p_X (e.g., Gaussian distribution or uniform distribution) to the underlying population distribution p_Y of the genuine sample, e.g., the MNIST or the ImageNet dataset. Nowadays, generative models have been widely-used for generating realistic images [12, 33], songs [4, 13] and videos [32, 53]. Besides generative models, OTM also plays essential roles in various machine learning applications, say color transfer [14, 41], shape match [50], transfer learning [10, 38] and natural language processing [38].

Despite its impressive performance, the computation of OTM is challenging for a large-scale sample with massive sample size and/or high dimensionality. Traditional methods for estimating the OTM includes finding a parametric map and using ordinary differential equations [8, 2]. To address the computational concern, recent developments of OTM estimation have been made based on solving linear programs [44, 37]. Let $\{\boldsymbol{x}_i\}_{i=1}^n \in \mathbb{R}^d$ and $\{\boldsymbol{y}_i\}_{i=1}^n \in \mathbb{R}^d$ be two samples from two continuous probability distributions functions p_X and p_Y, respectively. Estimating the OTM from p_X to p_Y by solving a linear program requiring $O(n^3 \log(n))$ computational time for fixed d [38, 47]. To alleviate the computational burden, some literature [11, 17, 1, 21] pursued fast computation approaches of the OTM objective, i.e., the Wasserstein distance. Another school of methods aims to estimate the OTM efficiently when d is small, including multi-scale approaches [35, 18] and dynamic formulations

33rd Conference on Neural Information Processing Systems (NeurIPS 2019), Vancouver, Canada.

[48, 36]. These methods utilize the space discretization, thus are generally not applicable in high-dimensional cases.

The random projection method (or known as the radon transformation method) is proposed to estimate OTMs efficiently when d is large [39, 40]. Such a method tackles the problem of estimating a d-dimensional OTM iteratively by breaking down the problem into a series of subproblems, each of which finds a one-dimensional OTM using projected samples. Denote $\mathbb{S}^{d-1}$ as the d-dimensional unit sphere. In each iteration, a random direction $\boldsymbol{\theta} \in \mathbb{S}^{d-1}$ is picked, and the one-dimensional OTM is then calculated between the projected samples $\{\boldsymbol{x}_i^\intercal \boldsymbol{\theta}\}_{i=1}^n$ and $\{\boldsymbol{y}_i^\intercal \boldsymbol{\theta}\}_{i=1}^n$. The collection of all the one-dimensional maps serves as the final estimate of the target OTM. The sliced method modifies the random projection method by considering a large set of random directions from $\mathbb{S}^{d-1}$ in each iteration [7, 42]. The "mean map" of the one-dimensional OTMs over these random directions is considered as a component of the final estimate of the target OTM. We call the random projection method, the sliced method, and their variants as the *projection-based approach*. Such an approach reduces the computational cost of calculating an OTM from $O(n^3 \log(n))$ to $O(Kn \log(n))$, where K is the number of iterations until convergence. However, there is no theoretical guideline on the order of K. In addition, the existing projection-based approaches usually require a large number of iterations to convergence or even fail to converge. We speculate that the slow convergence is because a randomly selected projection direction may not be "informative", leading to a one-dimensional OTM that failed to be a decent representation of the target OTM. We illustrate such a phenomenon through an illustrative example as follows.

An illustrative example. The left and right panels in Figure 1 illustrates the importance of choosing the "informative" projection direction in OTM estimation. The goal is to obtain the OTM ϕ^* which maps a source distribution p_X (colored in red) to a target distribution p_Y (colored in green). For each panel, we first randomly pick a projection direction (black arrow) and obtain the marginal distributions of p_X and p_Y (the bell-shaped curves), respectively. The one-dimensional OTM then can be calculated based on the marginal distributions. Applying such a map to the source distribution yields the transformed distribution (colored in blue). One can observe that the transformed distributions are significantly different from the target ones. Such an observation indicates that the one-dimensional OTM with respect to a random projection direction may fail to well-represent the target OTM. This observation motivates us to select the "informative" projection direction (red arrow), which yields a better one-dimensional OTM.

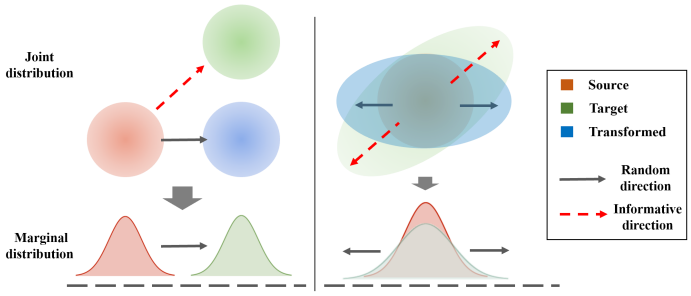

Figure 1: Illustration for the "informative" projection direction

Our contributions. To address the issues mentioned above, this paper introduces a novel statistical approach to estimate large-scale OTMs. The proposed method, named projection pursuit Monge map (PPMM), improves the existing projection-based approaches from two aspects. First, PPMM uses a sufficient dimension reduction technique to estimate the most "informative" projection direction in each iteration. Second, PPMM is based on projection pursuit [16]. The idea is similar to boosting that search for the next optimal direction based on the residual of previous ones. Theoretically, we show the proposed method can consistently estimate the most "informative" projection direction in each iteration, and the algorithm weakly convergences to the target large-scale OTM in a reasonable number of steps. The finite sample performance of the proposed algorithm is evaluated by two applications: Wasserstein distance estimation and generative model. We show the proposed method outperforms several state-of-the-art large-scale OTM estimation methods through extensive experiments on various synthetic and real-world datasets.

2 Problem setup and methodology

Optimal transport map and Wasserstein distance. Denote $X \in \mathbb{R}^d$ and $Y \in \mathbb{R}^d$ as two continuous random variables with probability distribution functions p_X and p_Y, respectively. The problem of finding a transport map $\phi : \mathbb{R}^d \to \mathbb{R}^d$ such that $\phi(X)$ and Y have the same distribution, has been

widely-studied in mathematics, probability, and economics, see [14, 50, 43] for examples of some new developments. Note that the transport map between the two distributions is not unique. Among all transport maps, it may be of interest to define the "optimal" one according to some criteria. A standard approach, named Monge formulation [52], is to find the OTM[1] ϕ^* that satisfies

$$\phi^* = \inf_{\phi \in \Phi} \int_{\mathbb{R}^d} \|X - \phi(X)\|^p \mathrm{d}p_X,$$

where Φ is the set of all transport maps, $\|\cdot\|$ is the vector norm and p is a positive integer. Given the existence of the Monge map, the Wasserstein distance of order p is defined as

$$W_p(p_X, p_Y) = \left(\int_{\mathbb{R}^d} \|X - \phi^*(X)\|^p \mathrm{d}p_X \right)^{1/p}.$$

Denote $\widehat{\phi}$ as an estimator of ϕ^*. Suppose one observe $\mathbf{X} = (\boldsymbol{x}_1, \ldots, \boldsymbol{x}_n)^\intercal \in \mathbb{R}^{n \times d}$ and $\mathbf{Y} = (\boldsymbol{y}_1, \ldots, \boldsymbol{y}_n)^\intercal \in \mathbb{R}^{n \times d}$ from p_X and p_Y, respectively. The Wasserstein distance $W_p(p_X, p_Y)$ thus can be estimated by

$$\widehat{W}_p(\mathbf{X}, \mathbf{Y}) = \left(\frac{1}{n} \sum_{i=1}^{n} \|\boldsymbol{x}_i - \widehat{\phi}(\boldsymbol{x}_i)\|^p \right)^{1/p}.$$

Projection pursuit method. Projection pursuit regression [16, 24, 15, 26] is widely-used for high-dimensional nonparametric regression models which takes the form.

$$z_i = \sum_{j=1}^{s} f_j(\boldsymbol{\beta}_j^\intercal \boldsymbol{x}_i) + \epsilon_i, \quad i = 1, \ldots, n, \tag{1}$$

where s is a hyper-parameter, $\{z_i\}_{i=1}^n \in \mathbb{R}$ is the univariate response, $\{\boldsymbol{x}_i\}_{i=1}^n \in \mathbb{R}^d$ are covariates, and $\{\epsilon_i\}_{i=1}^n$ are i.i.d. normal errors. The goal is to estimate the unknown link functions $\{f_j\}_{j=1}^s : \mathbb{R} \to \mathbb{R}$ and the unknown coefficients $\{\boldsymbol{\beta}_j\}_{j=1}^s \in \mathbb{R}^d$.

The additive model (1) can be fitted in an iterative fashion. In the kth iteration, $k = 2, \ldots, s$, denote $\{(\widehat{f}_j, \widehat{\boldsymbol{\beta}}_j)\}_{j=1}^{k-1}$ the estimate of $\{(f_j, \boldsymbol{\beta}_j)\}_{j=1}^{k-1}$ obtained from previous $k-1$ iterations. Denote $R_i^{[k]} = z_i - \sum_{j=1}^{k-1} \widehat{f}_j(\widehat{\boldsymbol{\beta}}_j^\intercal \boldsymbol{x}_i)$, $i = 1, \ldots, n$, the residuals. Then $(f_k, \boldsymbol{\beta}_k)$ can be estimated by solving the following least squares problem

$$\min_{f_k, \boldsymbol{\beta}_k} \sum_{i=1}^{n} \left[R_i^{[k]} - f_k(\boldsymbol{\beta}_k^\intercal \boldsymbol{x}_i) \right]^2.$$

The above iterative process explains the intuition behind the projection pursuit regression. Given the model fitted in previous iterations, we fit a one dimensional regression model using the current residuals, rather than the original responses. We then add this new regression model into the fitted function in order to update the residuals. By adding small regression models to the residuals, we gradually improve fitted model in areas where it does not perform well.

The intuition of projection pursuit regression motivates us to modify the existing projection-based OTM estimation approaches from two aspects. First, in the kth iteration, we propose to seek a new projection direction for the one-dimensional OTM in the subspace spanned by the residuals of the previously $k-1$ directions. On the contrary, following a direction that is in the span of used ones can lead to an inefficient one dimensional OTM. As a result, this "move" may hardly reduce the Wasserstein distance between p_X and p_Y. Such inefficient "moves" can be one of the causes of the convergence issue in existing projection-based OTM estimation algorithms. Second, in each iteration, we propose to select the most "informative" direction with respect to the current residuals rather than a random one. Specifically, we choose the direction that explains the highest proportion of variations in the subspace spanned by the current residuals. Intuitively, this direction addresses the maximum marginal "discrepancy" between p_X and p_Y among the ones that are not considered by previous iterations. We propose to estimate this most "informative" direction with sufficient dimension reduction techniques introduced as follows.

[1] Such a map is thus also called the Monge map.

Sufficient dimension reduction. Consider a regression problem with univariate response Z and a d-dimensional predictor X. Sufficient dimension reduction for regression aims to reduce the dimension of X while preserving its regression relation with Z. In other words, sufficient dimension reduction seeks a set of linear combinations of X, say $\mathbf{B}^\intercal X$ with some $\mathbf{B} \in \mathbb{R}^{d\times q}$ and $q \leq d$, such that Z depends on X only through $\mathbf{B}^\intercal X$, i.e., $Z \perp\!\!\!\perp X|\mathbf{B}^\intercal X$. Then, the column space of $\mathbf{B}$, denoted as $\mathcal{S}(\mathbf{B})$ is called a dimension reduction space (DRS). Furthermore, if the union of all possible DRSs is also a DRS, we call it the central subspace and denote it as $\mathcal{S}_{Z|X}$. When $\mathcal{S}_{Z|X}$ exists, it is the minimum DRS. We call a sufficient dimension reduction method exclusive if it induces a DRS that equals to the central subspace. Some popular sufficient dimension reduction techniques include sliced inverse regression (SIR) [30], principal Hessian directions (PHD) [31], sliced average variance estimator (SAVE) [9], directional regression (DR) [29], among others.

Estimation of the most "informative" projection direction. Consider estimating an OTM between a source sample and a target sample. We first form a regression problem by adding a binary response, which equals zero for the source sample and one for the target sample. We then utilize the sufficient dimension reduction technique to select the most "informative" projection direction. To be specific, we select the projection direction $\boldsymbol{\xi} \in \mathbb{R}^d$ as the eigenvector corresponds to the largest eigenvalue of the estimated $\mathbf{B}$. The direction $\boldsymbol{\xi}$ is most "informative" in the sense that, the projected samples $\mathbf{X}\boldsymbol{\xi}$ and $\mathbf{Y}\boldsymbol{\xi}$ have the most substantial " discrepancy." The metric of the "discrepancy" depends on the choice of the sufficient dimension reduction technique. Figure 2 gives a toy example to illustrate this idea. In this paper, we opt to use SAVE for calculating $\mathbf{B}$, and hence the "discrepancy" metric is the difference between $\text{Var}(\mathbf{X}\boldsymbol{\xi})$ and $\text{Var}(\mathbf{Y}\boldsymbol{\xi})$. Empirically, we find other sufficient dimension reduction techniques, like PHD and DR, also yield similar performance. The SIR method, however, yields inferior performance, since it only considers the first moment. The Algorithm 1 below introduces our estimation method of "informative" projection direction in detail.

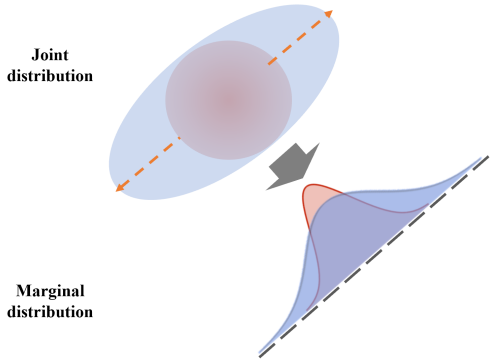

Figure 2: The most "informative" projection direction ensures the projected samples (illustrated by the distributions colored in red and blue, respectively) have the largest "discrepancy".

Algorithm 1 Select the most "informative" projection direction using SAVE

Input: two standardized matrix $\mathbf{X} \in \mathbb{R}^{n\times d}$ and $\mathbf{Y} \in \mathbb{R}^{n\times d}$

Step 1: calculate $\widehat{\boldsymbol{\Sigma}} \in \mathbb{R}^{d\times d}$, i.e., the sample variance-covariance matrix of $\binom{\mathbf{X}}{\mathbf{Y}}$

Step 2: calculate the sample variance-covariance matrices of $\mathbf{X}\widehat{\boldsymbol{\Sigma}}^{-1/2}$ and $\mathbf{Y}\widehat{\boldsymbol{\Sigma}}^{-1/2}$, denoted as $\widehat{\boldsymbol{\Sigma}}_1 \in \mathbb{R}^{d\times d}$ and $\widehat{\boldsymbol{\Sigma}}_2 \in \mathbb{R}^{d\times d}$, respectively

Step 3: calculate the eigenvector $\boldsymbol{\xi} \in \mathbb{R}^d$, which corresponding to the largest eigenvalue of the matrix $((\widehat{\boldsymbol{\Sigma}}_1 - I_d)^2 + (\widehat{\boldsymbol{\Sigma}}_2 - I_d)^2)/4$

Output: the final result is given by $\widehat{\boldsymbol{\Sigma}}^{-1/2}\boldsymbol{\xi}/||\widehat{\boldsymbol{\Sigma}}^{-1/2}\boldsymbol{\xi}||$, where $||\cdot||$ denotes the Euclidean norm

Projection pursuit Monge map algorithm. Now, we are ready to present our estimation method for large-scale OTM. The detailed algorithm, named projection pursuit Monge map, is summarized in Algorithm 2 below. In each iteration, the PPMM applies a one-dimensional OTM following the most "informative" projection direction selected by the Algorithm 1.

Computational cost of PPMM. In Algorithm 2, the computational cost mainly resides in the first two steps within each iteration. In step (a), one calculates $\boldsymbol{\xi}_k$ using Algorithm 1, whose computational cost is of order $O(nd^2)$. In step (b), one calculates a one-dimensional OTM using the look-up table, which is simply a sorting algorithm [40, 38].

The computational cost for step (b) is of order $O(n\log(n))$. Suppose that the algorithm converges after K iterations. The overall computational cost of Algorithm 2 is of order $O\left(Knd^2 + Kn\log(n)\right)$. Empirically, we find $K = O(d)$ works reasonably well. When $\log(n)^{1/2} \leq d \ll n^{2/3}$, the order of computational cost of PPMM is $o\left(n^3\log(n)\right)$ which is smaller than the computational cost of

Algorithm 2 Projection pursuit Monge map (PPMM)

Input: two matrix $\mathbf{X} \in \mathbb{R}^{n\times d}$ and $\mathbf{Y} \in \mathbb{R}^{n\times d}$
$k \leftarrow 0$, $\mathbf{X}^{[0]} \leftarrow \mathbf{X}$
repeat
(a) calculate the projection direction $\boldsymbol{\xi}_k \in \mathbb{R}^d$ between $\mathbf{X}^{[k]}$ and $\mathbf{Y}$ (using Algorithm 1)
(b) find the one-dimensional OTM $\phi^{(k)}$ that matches $\mathbf{X}^{[k]}\boldsymbol{\xi}_k$ to $\mathbf{Y}\boldsymbol{\xi}_k$ (using look-up table)
(c) $\mathbf{X}^{[k+1]} \leftarrow \mathbf{X}^{[k]} + (\phi^{(k)}(\mathbf{X}^{[k]}\boldsymbol{\xi}_k) - \mathbf{X}^{[k]}\boldsymbol{\xi}_k)\boldsymbol{\xi}_k^\intercal$ and $k \leftarrow k+1$
until converge
The final estimator is given by $\widehat{\phi} : \mathbf{X} \to \mathbf{X}^{[k]}$

the naive method for calculating OTMs. When $d \leq \log(n)^{1/2}$, the order of computational cost reduces to $O(Kn\log(n))$ which is faster than the exiting projection-based methods given PPMM converges faster. The memory cost for Algorithm 2 mainly resides in the step (a), which is of the order $O(Knd^2)$.

3 Theoretical results

Exclusiveness of SAVE. For mathematical simplicity, we assume $E[X] = E[Y] = \mathbf{0}_d$. When $E[X] \neq E[Y]$, one can use a first-order dimension reduction method like SIR to adjust means before applying SAVE.

Denote $W = (X+Y)/2$, $\Sigma_W = \mathrm{Var}(W)$, and $Z = W\Sigma_W^{-1/2}$. For a univariate continuous response variable R, one can approximate the central subspace $\mathcal{S}_{R|Z}$ by $\mathcal{S}_{\mathrm{SAVE}}$, which is the population version of the dimension reduction space of SAVE. To be specific, $\mathcal{S}_{\mathrm{SAVE}}$ is the column space of matrix

$$E[\mathrm{Var}(Z|R) - I_d]^2 = \frac{1}{4}\left\{E[\mathrm{Var}(X\Sigma_W^{-1/2}|R) - I_d]^2 + E[\mathrm{Var}(Y\Sigma_W^{-1/2}|R) - I_d]^2\right\},$$

where the above equation used the fact that $X \perp\!\!\!\perp Y$.

Assumption 1. *Let P be the projection onto the central space $\mathcal{S}_{R|Z}$ with respect to the inner project $a \cdot b = a^\intercal b$. For any nonzero vectors $u, v \in \mathbb{R}^d$, such that u is orthogonal to $\mathcal{S}_{R|Z}$ and $v \in \mathcal{S}_{R|Z}$, we assume*

(a) $E(u^\intercal Z|PZ)$ is a linear function of Z;
(b) $\mathrm{Var}(u^\intercal Z|PZ)$ is a nonrandom number;
(c) Let $(\widetilde{Z}, \widetilde{R})$ be an independent copy of (Z, R). $E\left[v^\intercal(Z-\widetilde{Z})^2|R, \widetilde{R})\right]$ is non degenerate; that is, it is not equal almost surely to a constant.

Theorem 1. *Let R be a univariate continuous response variable. Under Assumption 1, the dimension reduction space induced by SAVE is exclusive. In other words, $\mathcal{S}_{SAVE} = \mathcal{S}_{R|Z}$.*

Consistency of the most "informative" projection direction. Let $\widehat{\Sigma}_1$ and $\widehat{\Sigma}_2$ be the sample covariance matrix estimator of Σ_1 and Σ_2, respectively. Denote

$$\Sigma_{\mathrm{SAVE}} = \frac{1}{4}\left[(\Sigma_1 - I_d)^2 + (\Sigma_2 - I_d)^2\right] \quad \text{and} \quad \widehat{\Sigma}_{\mathrm{SAVE}} = \frac{1}{4}\left[(\widehat{\Sigma}_1 - I_d)^2 + (\widehat{\Sigma}_2 - I_d)^2\right].$$

Denote $\boldsymbol{\xi}_1$ and $\widehat{\boldsymbol{\xi}}_1$ the eigenvectors correspond to the largest eigenvalues of Σ_{SAVE} and $\widehat{\Sigma}_{\mathrm{SAVE}}$, respectively. Further, denote $r = \mathrm{Rank}(\Sigma_{\mathrm{SAVE}})$, the rank of Σ_{SAVE}.

Assumption 2. *Let $\{\boldsymbol{x}_i, \boldsymbol{y}_i\}_{i=1}^n$ be an i.i.d. sample of (X, Y). We assume that*

(a) Denote x_{ij} and y_{ik} the jth and kth component of $\boldsymbol{x}_i$ and $\boldsymbol{y}_i$, respectively. $E(x_{ij}y_{ik}) = 0$ for all $1 \leq i \leq n$ and $1 \leq j, k \leq d$;

(b) There are $r_1, r_2 > 0$ and $b_1, b_2 > 0$ such that, for any $s > 0$, $1 \leq i \leq n$ and $1 \leq j \leq d$,

$$P(|x_{ij}| > s) \leq \exp\{-(s/b_1)^{r_1}\} \quad \text{and} \quad P(|y_{ij}| > s) \leq \exp\{-(s/b_2)^{r_2}\};$$

(c) *Let* $\lambda_1 \ldots, \lambda_d$ *be the eigenvalues of* Σ_{SAVE} *in descending order. There exist positive constants* c_l c_u *and* c_3 *such that*

$$c_l \leq \min_{1 \leq l \leq r-1} (\lambda_l - \lambda_{l+1}) d^{-1/2} \leq c_u, \quad \textit{and} \quad 0 \leq \lambda_{r+1} < c_3.$$

Theorem 2 shows that Algorithm 1 can consistently estimate the most "informative" projection direction. The O_p in Theorem 2 stands for order in probability, which is similar to O but for random variables.

Theorem 2. *Under Assumption 2, the SAVE estimator of most "informative" projection direction satisfies,*

$$\|\widehat{\boldsymbol{\xi}}_1 - \boldsymbol{\xi}_1\|_\infty = O_p(r^4 \sqrt{\frac{\log d}{n}} + r^4 \sqrt{d} \frac{\log d}{n}), \quad \textit{as} \quad n, d \to \infty.$$

Weak convergence of PPMM algorithm. Denote ϕ^* as the d-dimensional optimal transport map from p_X to p_Y and $\phi^{(K)}$ as the PPMM estimator after K iterations, i.e. $\phi^{(K)}(\mathbf{X}) = \mathbf{X}^{[K]}$. The following theorem gives the weak convergence results of the PPMM algorithm.

Theorem 3. *Suppose Assumption 1 and Assumption 2 hold. Let* $K \geq Cd$ *for some large enough positive constant* C*, one has*

$$\widehat{W}_p\Big(\phi^{(K)}(\mathbf{X}), \mathbf{X}\Big) \to W_p\Big(\phi^*(X), X\Big), \quad \textit{and} \quad \phi^{(K)}(\mathbf{X}) \to \phi^*(X) \quad \textit{as} \quad n \to \infty.$$

Works are proving the convergence rates of the empirical optimal transport objectives [5, 49, 6, 54]. The convergence rate of the OTM has rarely been studied except for a recent paper [25]. We believe Theorem 3 is the first step in this direction.

4 Numerical experiments

4.1 Estimation of optimal transport map

Suppose that we observe i.i.d. samples $\mathbf{X} = (\boldsymbol{x}_1, \ldots, \boldsymbol{x}_n)^\intercal$ from $p_X = \mathcal{N}_d(\boldsymbol{\mu}_X, \boldsymbol{\Sigma}_X)$ and $\mathbf{Y} = (\boldsymbol{y}_1, \ldots, \boldsymbol{y}_n)^\intercal$ from $p_Y = \mathcal{N}_d(\boldsymbol{\mu}_Y, \boldsymbol{\Sigma}_Y)$, respectively. We set $n = 10,000$, $d = \{10, 20, 50\}$, $\boldsymbol{\mu}_X = -\mathbf{2}$, $\boldsymbol{\mu}_Y = \mathbf{2}$, $\boldsymbol{\Sigma}_X = 0.8^{|i-j|}$, and $\boldsymbol{\Sigma}_Y = 0.5^{|i-j|}$, for $i, j = 1, \ldots, d$.

We apply PPMM to estimate the OTM between p_X and p_Y from $\{\boldsymbol{x}_i\}_{i=1}^n$ and $\{\boldsymbol{y}_i\}_{i=1}^n$. In comparison, we also consider the following two projection-based competitors: (1) the random projection method (RANDOM) as proposed in [39, 40]; (2) the sliced method as proposed in [7, 42]. The number of slices L is set to be 10, 20, and 50. We assess the convergence of each method by the estimated Wasserstein distance of order 2 after each iteration, i.e. $\widehat{W}_2\Big(\phi^{(k)}(\mathbf{X}), \mathbf{X}\Big)$, where $\phi^{(k)}(\cdot)$ is the estimator of OTM after kth iteration. For all three methods, we set the maximum number of iterations to be 200. Notice that, the Wasserstein distance between p_X and p_Y admits a closed form,

$$W_2^2(p_X, p_Y) = ||\boldsymbol{\mu}_X - \boldsymbol{\mu}_Y||_2^2 + trace\left(\boldsymbol{\Sigma}_X + \boldsymbol{\Sigma}_Y - 2(\boldsymbol{\Sigma}_X^{1/2} \boldsymbol{\Sigma}_Y \boldsymbol{\Sigma}_X^{1/2})^{1/2}\right), \tag{2}$$

which serves as the ground-truth. The results are presented in Figure 3.

In all three scenarios, PPMM (red line) converges to the ground truth within a small number of iterations. The fluctuations of the convergence curves observed in Figure 3 are caused by the non-equal sample means. This can be adjusted by applying a first-order dimension reduction method (e.g., SIR). We do not pursue this approach as the fluctuations do not cover the main pattern in Figure 3. When $d = 10$, RANDOM and SLICED converge to the ground truth but in a much

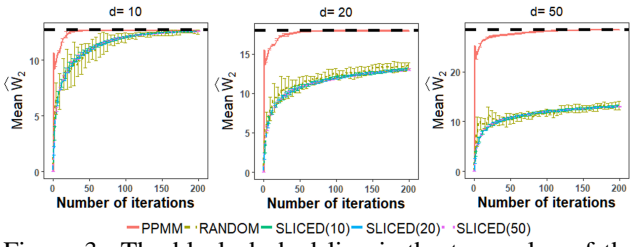

Figure 3: The black dashed line is the true value of the Wasserstein distance as in (2). The colored lines represent the sample mean of the estimated Wasserstein distances over 100 replications, and the vertical bars represent the standard deviations.

slower manner. When $d = 20$ and 50, neither RANDOM nor SLICED manages to converge within 200 iterations. We also find a large number of slices L does not necessarily lead to a better estimation for the SLICED method. As we can see, PPMM is the only one among three that is adaptive to large-scale OTM estimation problems.

In Table 1 below, we compare the computational cost of three methods by reporting the CPU time per iteration over 100 replication.[2] As we expected, the RANDOM method has the lowest CPU time per iteration due to it does not select projection direction. We notice that the CPU time per iteration of the SLICED method is proportional to the number of slices L. Last but not least, the CPU time per iteration of PPMM is slightly larger than RANDOM but much smaller than SLICED.

Table 1: The mean CPU time (sec) per iteration, with standard deviations presented in parentheses

	PPMM	RANDOM	SLICED(10)	SLICED(20)	SLICED(50)
$d = 10$	0.019 (0.008)	0.011 (0.008)	0.111 (0.019)	0.213 (0.024)	0.529 (0.031)
$d = 20$	0.027 (0.011)	0.014 (0.008)	0.125 (0.027)	0.247 (0.033)	0.605 (0.058)
$d = 50$	0.059 (0.036)	0.015 (0.008)	0.171 (0.037)	0.338 (0.049)	0.863 (0.117)

In the Table 2 below, we report the mean convergence time over 100 replications for PPMM, RANDOM, SLICED, the refined auction algorithm (AUCTIONBF)[3], the revised simplex algorithm (REVSIM) [34] and the shortlist method (SHORTSIM) [20].[3] Table 2 shows that the PPMM is the most computationally efficient method thanks to its cheap per iteration cost and fast convergence.

Table 2: The mean convergence time (sec) for estimating the Wasserstein distance, with standard deviations presented in parentheses. The symbol "-" is inserted when the algorithm fails to converge.

	PPMM	RANDOM	SLICED(10)	AUCTIONBF	REVSIM	SHORTSIM
$d = 10$	0.6 (0.1)	4.8 (1.7)	23.0 (2.6)	99.7 (10.4)	40.2 (4.0)	42.5 (3.2)
$d = 20$	2.1 (0.3)	24.4 (3.2)	230.2 (28.4)	109.4 (12.5)	42.6 (5.3)	50.2 (6.6)
$d = 50$	5.5 (0.4)	-	-	125.5 (13.3)	46.5 (5.6)	56.5 (7.1)

4.2 Application to generative models

A critical issue in generative models is the so-called mode collapse, i.e., the generated "fake" sample fails to capture some modes present in the training data [22, 45]. To address this issue, recent studies [51, 22, 28] incorporated generative models with the optimal transportation theory. As illustrated in Figure 4, one can decompose the problem of generating fake samples into two major steps: (1) manifold learning and (2) probability transformation. The step (1) aims to discover the manifold structure of the training data by mapping the training data from the original space $\mathcal{X} \subset \mathbb{R}^d$ to a latent space $\mathcal{Z} \subset \mathbb{R}^{d^*}$ with $d^* \ll d$. Notice that the probability distribution of the transformed data in $\mathcal{Z}$ may not be convex, leading to the problem of mode collapse. The step (2) then addresses the mode collapse issue through transporting the distribution in $\mathcal{Z}$ to the uniform distribution $U([0,1]^{d^*})$. Then, the generative model takes a random input from $U([0,1]^{d^*})$ and sequentially applies the inverse transformations in step (2) and step (1) to generate the output. In practice, one may implement the step (1) and (2) using variational autoencoders (VAE) and OTM, respectively. As we can see, the estimation of OTM plays an essential role in this framework.

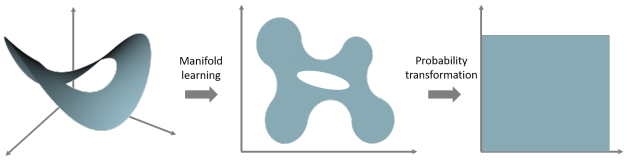

Figure 4: Illustration for the generative model using manifold learning and optimal transport

In this subsection, we apply PPMM as well as RANDOM and SLICED to generative models to study two datasets: MINST and Google doodle dataset. For the SLICED method, we set the number of slices to be 10, 20, and 50. For all three methods, we set the number of iterations is set to be $10d^*$. We use the squared Euclidean distance as the cost for the VAE model.

[2]The experiments are implemented by an Intel 2.6 GHz processor.

[3]AUCTIONBF, REVSIM and SHORTSIM are implemented by the R package "transport" [46].

Table 3: The FID for the generated samples (lower the better), with standard deviations presented in parentheses

	PPMM	RANDOM	SLICED(10)	SLICED(20)	SLICED(50)
MNIST	**0.17** (0.01)	4.62 (0.02)	2.98 (0.01)	3.04 (0.01)	3.12 (0.01)
Doodle (face)	**0.59** (0.09)	8.78 (0.04)	5.69 (0.01)	6.01 (0.01)	5.52 (0.01)
Doodle (cat)	**0.24** (0.03)	8.93 (0.03)	5.99 (0.01)	5.26 (0.01)	5.33 (0.01)
Doodle (bird)	**0.36** (0.03)	7.81 (0.03)	5.44 (0.01)	5.50 (0.01)	4.98 (0.01)

MNIST. We first study the MNIST dataset, which contains 60,000 training images and 10,000 testing images of hand written digits. We pull each 28×28 image to a 784-dimensional vector and rescale the grayscale values from $[0, 255]$ to $[0, 1]$. Following the method in [51], we apply VAE to encode the data into a latent space $\mathcal{Z}$ of dimensionality $d^* = 8$. Then, the OTM from the distribution in $\mathcal{Z}$ to $U([0, 1]^8)$ is estimated by PPMM as well as RANDOM and SLICED.

Figure 5: Left: random samples generated by PPMM. Right: linear interpolation between random pairs of images.

First, we visually examine the fake sample generated with PPMM. In the left-hand panel of Figure 5, we display some random images generated by PPMM. The right-hand panel of Figure 5 shows that PPMM can predict the continuous shift from one digit to another. To be specific, let $\boldsymbol{a}, \boldsymbol{b} \in \mathbb{R}^{784}$ be the sample of two digits (e.g. 3 and 9) in the testing set. Let $T : \mathcal{X} \to \mathcal{Z}$ be the map induced by VAE and $\widehat{\phi}$ the OTM estimated by PPMM. Then, $\widehat{\phi}(T(\cdot))$ maps the sample distribution to $U([0, 1]^8)$. We linearly interpolate between $\widehat{\phi}(T(\boldsymbol{a}))$ and $\widehat{\phi}(T(\boldsymbol{b}))$ with equal-size steps. Then we transform the interpolated points back to the sample distribution to generate the middle columns in the right panel of Figure 5.

We use the *"Fréchet Inception Distance"* (FID) [23] to quantify the similarity between the generated fake sample and the training sample. Specifically, we first generate 1,000 random inputs from $U([0, 1]^8)$. We then apply PPMM, RANDOM, and SLICED to this input sample, yields the fake samples in the latent space $\mathcal{Z}$. Finally, we calculate the FID between the encoded training sample in the latent space and the generated fake samples, respectively. A small value of FID indicates the generated fake sample is similar to the training sample and vice versa. The sample mean and sample standard deviation (in parentheses) of FID over 50 replications are presented in Table 3. Table 3 indicates PPMM significantly outperforms the other two methods in terms of estimating the OTM.

Google doodle dataset. The Google Doodle dataset[4] contains over 50 million drawings created by users with a mouse under 20 secs. We analyze a pre-processed version of this dataset from the quick draw Github account[5]. In the dataset we use, the drawings are centered and rendered into 28×28 grayscale images. We pull each 28×28 image to a 784-dimensional vector and rescale the grayscale values from $[0, 255]$ to $[0, 1]$. In this experiment, we study the drawings from three different categories: smile face, cat, and bird. These three categories contain 161,666, 123,202, and 133,572 drawings, respectively. Within each category, we randomly split the data into a training set and a validation set of equal sample sizes.

We apply VAE to the training set with a stopping criterion selected by the validation set. The dimension of the latent space is set to be 16. Let $\boldsymbol{a}, \boldsymbol{b} \in \mathbb{R}^{784}$ be two vectors in the validation set, $T : \mathcal{X} \to \mathcal{Z}$ be the map induced by VAE and $\widehat{\phi}$ be the OTM estimated by PPMM. Note that $\widehat{\phi}(T(\cdot))$ maps the sample distribution to $U([0, 1]^{16})$. We then linearly interpolate between $\widehat{\phi}(T(\boldsymbol{a}))$ and $\widehat{\phi}(T(\boldsymbol{b}))$ with equal-size steps. The results are presented in Figure 6.

[4]https://quickdraw.withgoogle.com/data

[5]https://github.com/googlecreativelab/quickdraw-dataset

Figure 6: Linear interpolation between random pairs of images from the dataset of smile face (left), cat (center), and bird (right).

Then, we quantify the similarity between the generated fake samples and the truth by calculating the FID in the latent space. The sample mean and sample standard deviation (in parentheses) of FID over 50 replications are presented in Table 3. Again, the results in Table 3 justify the superior performance of PPMM over existing projection-based methods.

5 Extensions

First, the PPMM can be extended to address the penitential heterogeneous in the dataset by assigning non-equal weights to the points in source and target samples. This is equivalent to calculate weighted variance-covariance matrices in Step 2 of Algorithm 1. Second, the PPMM method can be modified to allow the sizes of the source and target samples to be different. In such a scenario, we can replace the look-up table in the Step (b) of Algorithm 2 with an approximate lookup table. Recall that the one-dimensional lookup table is just sorting, the one-dimensional approximate look-up table can be achieved by combining sorting and linear interpolation. We validate the above extensions with a simulated experiment similar to the one in Section 4.1 except that we draw $5,000$ and $1,000$ points from p_X and p_Y, respectively. We set $d = 10$ and assign weights to the observations randomly. The estimation results are presented in Figure 7. In addition, the average convergence time is: PPMM(0.3s), RANDOM (1.4s), SLICED10 (14s) and SHORTSIM (74s).

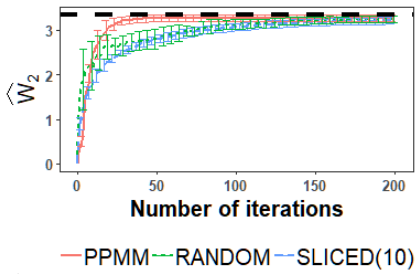

Figure 7: Experiment for heterogeneous data with non-equal sample sizes. The black dashed line is the oracle calculated by SHORTSIM

Theorem 3 suggests that, for the PPMM algorithm, the number of iterations until converge, i.e., K, is on the order of dimensionality d. Here we use a simulated example to assess whether this order is attainable. We follow a similar setting as in Section 4.1 except that we increase d from 10 to 100 with a step size of 10. Besides, we set the termination criteria to be a hard threshold, i.e., 10^{-5}. In Figure 8, we report the sample mean (solid line) and standard deviation (vertical bars) of K over 100 replications with respect to the increased d. One can observe a clear linear pattern.

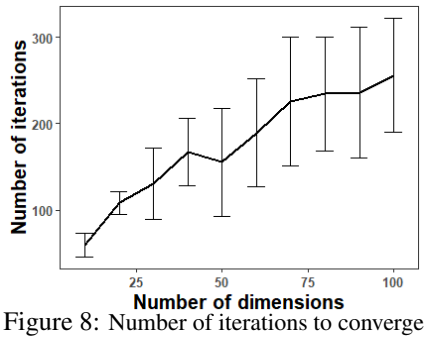

Figure 8: Number of iterations to converge

Acknowledgment

We would like to thank Xiaoxiao Sun, Rui Xie, Xinlian Zhang, Yiwen Liu, and Xing Xin for many fruitful discussions. We would also like to thank Dr. Xianfeng David Gu for his insightful blog about the Optimal transportation theory. Also, we would like to thank the UC Irvine Machine Learning Repository for dataset assistance. This work was partially supported by National Science Foundation grants DMS-1440037, DMS-1440038, DMS-1438957, and NIH grants R01GM113242, R01GM122080.

References

[1] M. Arjovsky, S. Chintala, and L. Bottou. Wasserstein generative adversarial networks. In *International Conference on Machine Learning*, pages 214–223, 2017.

[2] J.-D. Benamou, Y. Brenier, and K. Guittet. The monge–kantorovitch mass transfer and its computational fluid mechanics formulation. *International Journal for Numerical methods in fluids*, 40(1-2):21–30, 2002.

[3] D. P. Bertsekas. Auction algorithms for network flow problems: A tutorial introduction. *Computational optimization and applications*, 1(1):7–66, 1992.

[4] M. Blaauw and J. Bonada. Modeling and transforming speech using variational autoencoders. In *Interspeech*, pages 1770–1774, 2016.

[5] E. Boissard et al. Simple bounds for the convergence of empirical and occupation measures in 1-wasserstein distance. *Electronic Journal of Probability*, 16:2296–2333, 2011.

[6] E. Boissard and T. Le Gouic. On the mean speed of convergence of empirical and occupation measures in wasserstein distance. In *Annales de l'IHP Probabilités et statistiques*, volume 50, pages 539–563, 2014.

[7] N. Bonneel, J. Rabin, G. Peyré, and H. Pfister. Sliced and radon wasserstein barycenters of measures. *Journal of Mathematical Imaging and Vision*, 51(1):22–45, 2015.

[8] Y. Brenier. A homogenized model for vortex sheets. *Archive for Rational Mechanics and Analysis*, 138(4):319–353, 1997.

[9] R. D. Cook and S. Weisberg. Sliced inverse regression for dimension reduction: Comment. *Journal of the American Statistical Association*, 86(414):328–332, 1991.

[10] N. Courty, R. Flamary, D. Tuia, and A. Rakotomamonjy. Optimal transport for domain adaptation. *IEEE transactions on pattern analysis and machine intelligence*, 39(9):1853–1865, 2017.

[11] M. Cuturi. Sinkhorn distances: Lightspeed computation of optimal transport. In *Advances in neural information processing systems*, pages 2292–2300, 2013.

[12] A. Dosovitskiy and T. Brox. Generating images with perceptual similarity metrics based on deep networks. In *Advances in neural information processing systems*, pages 658–666, 2016.

[13] J. Engel, C. Resnick, A. Roberts, S. Dieleman, M. Norouzi, D. Eck, and K. Simonyan. Neural audio synthesis of musical notes with wavenet autoencoders. In *Proceedings of the 34th International Conference on Machine Learning-Volume 70*, pages 1068–1077. JMLR. org, 2017.

[14] S. Ferradans, N. Papadakis, G. Peyré, and J.-F. Aujol. Regularized discrete optimal transport. *SIAM Journal on Imaging Sciences*, 7(3):1853–1882, 2014.

[15] J. H. Friedman. Exploratory projection pursuit. *Journal of the American statistical association*, 82(397):249–266, 1987.

[16] J. H. Friedman and W. Stuetzle. Projection pursuit regression. *Journal of the American statistical Association*, 76(376):817–823, 1981.

[17] A. Genevay, M. Cuturi, G. Peyré, and F. Bach. Stochastic optimization for large-scale optimal transport. In *Advances in neural information processing systems*, pages 3440–3448, 2016.

[18] S. Gerber and M. Maggioni. Multiscale strategies for computing optimal transport. *The Journal of Machine Learning Research*, 18(1):2440–2471, 2017.

[19] I. Goodfellow, J. Pouget-Abadie, M. Mirza, B. Xu, D. Warde-Farley, S. Ozair, A. Courville, and Y. Bengio. Generative adversarial nets. In *Advances in neural information processing systems*, pages 2672–2680, 2014.

[20] C. Gottschlich and D. Schuhmacher. The shortlist method for fast computation of the earth mover's distance and finding optimal solutions to transportation problems. *PloS one*, 9(10):e110214, 2014.

[21] I. Gulrajani, F. Ahmed, M. Arjovsky, V. Dumoulin, and A. C. Courville. Improved training of wasserstein gans. In *Advances in Neural Information Processing Systems*, pages 5769–5779, 2017.

[22] Y. Guo, D. An, X. Qi, Z. Luo, S.-T. Yau, X. Gu, et al. Mode collapse and regularity of optimal transportation maps. *arXiv preprint arXiv:1902.02934*, 2019.

[23] M. Heusel, H. Ramsauer, T. Unterthiner, B. Nessler, and S. Hochreiter. Gans trained by a two time-scale update rule converge to a local nash equilibrium. In *Advances in Neural Information Processing Systems*, pages 6626–6637, 2017.

[24] P. J. Huber. Projection pursuit. *The annals of Statistics*, pages 435–475, 1985.

[25] J.-C. Hütter and P. Rigollet. Minimax rates of estimation for smooth optimal transport maps. *arXiv preprint arXiv:1905.05828*, 2019.

[26] A. Ifarraguerri and C.-I. Chang. Unsupervised hyperspectral image analysis with projection pursuit. *IEEE Transactions on Geoscience and Remote Sensing*, 38(6):2529–2538, 2000.

[27] D. P. Kingma and M. Welling. Auto-encoding variational bayes. *arXiv preprint arXiv:1312.6114*, 2013.

[28] S. Kolouri, P. E. Pope, C. E. Martin, and G. K. Rohde. Sliced-wasserstein autoencoder: An embarrassingly simple generative model. *arXiv preprint arXiv:1804.01947*, 2018.

[29] B. Li and S. Wang. On directional regression for dimension reduction. *Journal of the American Statistical Association*, 102(479):997–1008, 2007.

[30] K.-C. Li. Sliced inverse regression for dimension reduction. *Journal of the American Statistical Association*, 86(414):316–327, 1991.

[31] K.-C. Li. On principal hessian directions for data visualization and dimension reduction: Another application of stein's lemma. *Journal of the American Statistical Association*, 87(420):1025–1039, 1992.

[32] X. Liang, L. Lee, W. Dai, and E. P. Xing. Dual motion gan for future-flow embedded video prediction. In *Proceedings of the IEEE International Conference on Computer Vision*, pages 1744–1752, 2017.

[33] Y. Liu, Z. Qin, Z. Luo, and H. Wang. Auto-painter: Cartoon image generation from sketch by using conditional generative adversarial networks. *arXiv preprint arXiv:1705.01908*, 2017.

[34] D. G. Luenberger, Y. Ye, et al. *Linear and nonlinear programming*, volume 2. Springer, 1984.

[35] Q. Mérigot. A multiscale approach to optimal transport. In *Computer Graphics Forum*, volume 30, pages 1583–1592. Wiley Online Library, 2011.

[36] N. Papadakis, G. Peyré, and E. Oudet. Optimal transport with proximal splitting. *SIAM Journal on Imaging Sciences*, 7(1):212–238, 2014.

[37] O. Pele and M. Werman. Fast and robust earth mover's distances. In *2009 IEEE 12th International Conference on Computer Vision*, pages 460–467. IEEE, 2009.

[38] G. Peyré, M. Cuturi, et al. Computational optimal transport. *Foundations and Trends® in Machine Learning*, 11(5-6):355–607, 2019.

[39] F. Pitie, A. C. Kokaram, and R. Dahyot. N-dimensional probability density function transfer and its application to color transfer. In *Computer Vision, 2005. ICCV 2005. Tenth IEEE International Conference on*, volume 2, pages 1434–1439. IEEE, 2005.

[40] F. Pitié, A. C. Kokaram, and R. Dahyot. Automated colour grading using colour distribution transfer. *Computer Vision and Image Understanding*, 107(1-2):123–137, 2007.

[41] J. Rabin, S. Ferradans, and N. Papadakis. Adaptive color transfer with relaxed optimal transport. In *2014 IEEE International Conference on Image Processing (ICIP)*, pages 4852–4856. IEEE, 2014.

[42] J. Rabin, G. Peyré, J. Delon, and M. Bernot. Wasserstein barycenter and its application to texture mixing. In *International Conference on Scale Space and Variational Methods in Computer Vision*, pages 435–446. Springer, 2011.

[43] S. Reich. A nonparametric ensemble transform method for bayesian inference. *SIAM Journal on Scientific Computing*, 35(4):A2013–A2024, 2013.

[44] Y. Rubner, L. J. Guibas, and C. Tomasi. The earth mover's distance, multi-dimensional scaling, and color-based image retrieval. In *Proceedings of the ARPA image understanding workshop*, volume 661, page 668, 1997.

[45] T. Salimans, H. Zhang, A. Radford, and D. Metaxas. Improving gans using optimal transport. *arXiv preprint arXiv:1803.05573*, 2018.

[46] D. Schuhmacher, B. Bähre, C. Gottschlich, V. Hartmann, F. Heinemann, and B. Schmitzer. *Transport: Computation of Optimal Transport Plans and Wasserstein Distances*, 2019. R package version 0.12-1.

[47] V. Seguy, B. B. Damodaran, R. Flamary, N. Courty, A. Rolet, and M. Blondel. Large-scale optimal transport and mapping estimation. *arXiv preprint arXiv:1711.02283*, 2017.

[48] J. Solomon, R. Rustamov, L. Guibas, and A. Butscher. Earth mover's distances on discrete surfaces. *ACM Transactions on Graphics (TOG)*, 33(4):67, 2014.

[49] B. K. Sriperumbudur, K. Fukumizu, A. Gretton, B. Schölkopf, G. R. Lanckriet, et al. On the empirical estimation of integral probability metrics. *Electronic Journal of Statistics*, 6:1550–1599, 2012.

[50] Z. Su, Y. Wang, R. Shi, W. Zeng, J. Sun, F. Luo, and X. Gu. Optimal mass transport for shape matching and comparison. *IEEE transactions on pattern analysis and machine intelligence*, 37(11):2246–2259, 2015.

[51] I. Tolstikhin, O. Bousquet, S. Gelly, and B. Schoelkopf. Wasserstein auto-encoders. *arXiv preprint arXiv:1711.01558*, 2017.

[52] C. Villani. *Optimal transport: old and new*. Springer Science & Business Media, 2008.

[53] C. Vondrick, H. Pirsiavash, and A. Torralba. Generating videos with scene dynamics. In *Advances In Neural Information Processing Systems*, pages 613–621, 2016.

[54] J. Weed and F. Bach. Sharp asymptotic and finite-sample rates of convergence of empirical measures in wasserstein distance. *arXiv preprint arXiv:1707.00087*, 2017.